
Article:
Sharma, A., Tripathi, D., Erdelyi, R. orcid.org/0000-0003-3439-4127 et al. (2 more authors) (2020) Wave amplitude modulation in fan loops as observed by AIA/SDO. Astronomy and Astrophysics, 638. A6. ISSN 0004-6361

https://doi.org/10.1051/0004-6361/201936667

A&A 638, A6 (2020)
https://doi.org/10.1051/0004-6361/201936667

Astronomy & Astrophysics

Wave amplitude modulation in fan loops as observed by AIA/SDO

Aishawnnya Sharma[1,2], Durgesh Tripathi[1], Robertus Erdélyi[3,4], Girjesh R. Gupta[5], and Gazi A. Ahmed[2]

[1] Inter-University Centre for Astronomy and Astrophysics, Post Bag-4, Ganeshkhind, Pune 411007, India
e-mail: aish@iucaa.in
[2] Department of Physics, Tezpur University, Tezpur 784028, India
[3] Solar Physics and Space Plasma Research Centre (SP^{2}RC), School of Mathematics and Statistics, University of Sheffield, Hicks Building, Hounsfield Road, Sheffield S3 7RH, UK
[4] Department of Astronomy, Eötvös Loránd University, Pázmány P. sétány 1/A, Budapest, H-117, Hungary
[5] Udaipur Solar Observatory, Physical Research Laboratory, Badi Road, Devali, Udaipur 313001, India

Received 10 September 2019 / Accepted 30 March 2020

ABSTRACT

Aims. We perform a detailed analysis to understand the evolution and dynamics of propagating intensity disturbances observed in a fan loop system.
Methods. We performed multiwavelength time-distance analysis of a fan loop system anchored in an isolated sunspot region (*AR 12553*). The active region was observed by the Atmospheric Imaging Assembly on board the Solar Dynamics Observatory. We measured the phase speeds of the propagating intensity disturbances by employing cross-correlation analysis, and by obtaining the slopes in xt-plots. We obtained original and detrended light curves at different heights of the time-distance maps and characterised them by performing Fourier and wavelet analysis, respectively.
Results. The time-distance maps reveal clear propagation of intensity oscillations in all the coronal extreme ultraviolet (EUV) channels except AIA 94 and 335 Å. We determine the nature of the intensity disturbances as slow magneto-acoustic waves by measuring their phase speeds. The time-distance maps, as well as the detrended light curves, show an increase and decrease in the amplitude of propagating 3 min oscillations over time. The amplitude variations appear most prominently in AIA 171 Å, though other EUV channels also show such signatures. The Fourier power spectrum yields the presence of significant powers with several nearby frequencies in the range of 2–3 min (5–8 mHz), along with many other smaller peaks between 2–4 min. Wavelet analysis shows an increase and decrease of oscillating power around 3 min simultaneous to the amplitude variations. We obtain the modulation period to be in the range of 20–30 min.
Conclusions. Our results provide the viability of occurrence of phenomenon like "Beat" among the nearby frequencies giving rise to the observed amplitude modulation. However, we cannot at this stage rule out the possibility that the modulation may be driven by variability in an underlying unknown source.

Key words. Sun: atmosphere – Sun: corona – Sun: oscillations – waves – Sun: UV radiation

1. Introduction

The identification and characterisation of magnetohydrodynamic (MHD) waves and oscillations are major areas of research in the field of solar plasma-astrophysics. MHD waves are considered to be an important candidate for heating of the solar atmosphere (Erdélyi 2004; Ofman 2005; Taroyan & Erdélyi 2009; Rajaguru et al. 2019; Liu et al. 2019). They may have significant roles in triggering jets (De Pontieu et al. 2004; Chandra et al. 2015) and in the acceleration of fast solar wind (Cranmer 2009).

One of the wave modes observed in the solar corona is slow mode magneto-acoustic waves. The propagation of this wave mode is largely confined to the magnetic field direction. They are compressional in nature, and propagate at a speed that is lower than the local sound speed in the solar corona. These waves are often observed as fluctuations in intensity and in Doppler velocity (Wang et al. 2009; Gupta et al. 2012). These waves were first reported as propagating intensity disturbances (PIDs) by Ofman et al. (1997) in coronal plumes in off-limb observations recorded by the UltraViolet Coronagraph Spectrometer (UVCS, Kohl et al. 1995) on board the Solar and Heliospheric Observatory (SOHO). Similar intensity oscillations in coronal fan loops were first detected by Berghmans & Clette (1999) using the Extreme ultraviolet Imaging Telescope (EIT, Delaboudinière et al. 1995) on board SOHO in 195 Å channel, and later confirmed by De Moortel et al. (2000) in the observations recorded by Transition Region and Coronal Explorer (TRACE, Handy et al. 1999) in the 171 Å channel. Fan loops are magnetic plasma structures in the corona with temperature between 0.6–1 MK (Reale 2010; Ghosh et al. 2017). They are found at the edges of active regions, and are mostly rooted in the umbra and umbra–penumbra boundaries of sunspots. They also remain anchored to the penumbra and non-sunspot (e.g. plage) regions. From a statistical study, Kiddie et al. (2012) concluded that PIDs of sunspot origin are temperature dependent and have subsonic propagation speed.

Since the discovery of PIDs in coronal fan loops, a number of theoretical and observational studies have been performed to unravel their characteristics, propagation, and dissipation and also their counterparts in the lower solar atmosphere (see e.g. Nakariakov et al. 2000; De Moortel et al. 2002a,b; Roberts 2006; De Moortel 2009; Bogdan 2000; Bogdan & Judge 2006; Khomenko & Collados 2015). Using wavelet analysis, De Moortel et al. (2002c) found that the periods of the PIDs are of the order of 282 ± 93 s. However, careful observation of their footpoint locations showed that the coronal fan loops rooted in

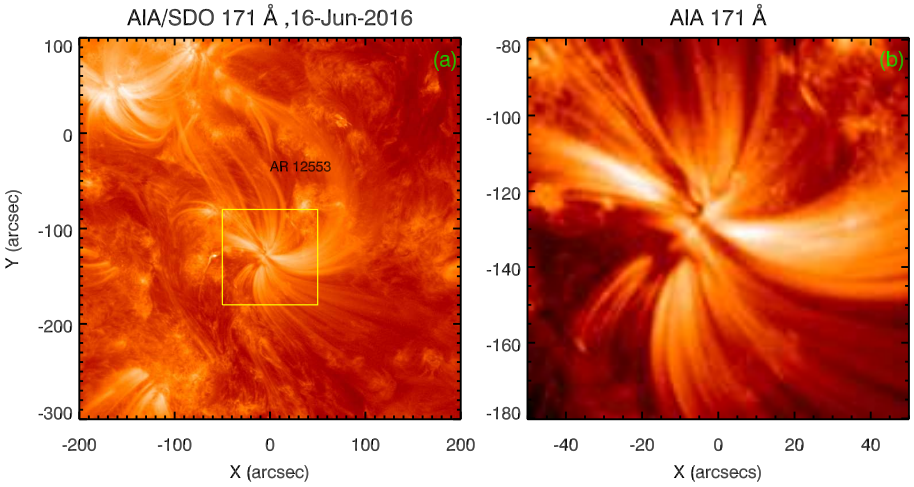

Fig. 1. *Panel a*: AIA 171 Å image showing the active region. The yellow box encloses the fan loop system, the region of interest studied in this paper. *Panel b*: zoomed-in image corresponding to the yellow box shown in panel a.

sunspot regions have a dominant period of 172 ± 32 s, and the loops rooted in non-sunspot regions such as plages are dominant in 321 ± 74 s period oscillations. This distinction was explained in terms of the underlying driver at the photospheric level exciting the loop footpoints.

In addition to the regular 3 min and 5 min oscillation, a few studies have reported longer period oscillations in the fan loops. Wang et al. (2009) has reported longer-period propagating waves at around 12 and 25 min along a fan-like coronal structure in the intensity (see also Marsh et al. 2009) and Doppler shift of the Fe XII 195 Å line using the Extreme ultraviolet Imaging Spectrometer (EIS, Culhane et al. 2007) on board *Hinode* (Kosugi et al. 2007). Stenborg et al. (2011) showed the presence of waves in coronal fan loops in multiples of 8 min (e.g. 16 min, 24 min, 40 min). It was speculated that the presence of the 8 min period could be attributed to the beat phenomenon, which may occur due to the superposition of ubiquitous 3 min chromospheric and 5 min photospheric oscillations that leak into the corona through the inclined guide field that is provided by fan loops. However, they did not emphasise the excitation mechanisms of other longer period oscillations that they detected in their observations.

In this paper, we perform a detailed analysis of intensity perturbations propagating along a fan loop system anchored within a sunspot. We track the evolution of these intensity oscillations by using the high spatially and temporally resolved data recorded by the Atmospheric Imaging Assembly (AIA, Lemen et al. 2012) on board the Solar Dynamic Observatory (SDO, Pesnell et al. 2012). Our motivation is to understand how intensity oscillations with a range of periodicities interact, and how they affect the propagation characteristics of most dominant 3 min oscillations along fan loops. The rest of the paper is structured as follows. In Sect. 2, we describe the observations obtained for this study and briefly address the data reduction and preparation. We present the details of the different analyses acquired in this study, such as time-distance maps, Fourier analysis, and wavelet analysis, and the results in Sect. 3. Finally, we summarise our findings and conclude in Sect. 4.

2. Observations

The main aim of this work is to perform a multiwavelength study of the dynamics of a fan loop system. For this purpose we used the observations recorded by AIA using its UV channel, AIA 1600 Å, and all the extreme ultraviolet (EUV) channels, AIA 304 Å, 171 Å, 131 Å, 193 Å, 211 Å, 335 Å, and 94 Å. These channels are dominated with different spectral lines formed in a range of temperatures. For more information on the temperature sensitivity of different channels see O'Dwyer et al. (2010), Del Zanna et al. (2011), and Boerner et al. (2012). AIA provides full-disk images with a cadence of 12 s in EUV and 24 s in UV. In addition, for contextual purpose, we use continuum data obtained using the Helioseismic and Magnetic Imager (HMI, Schou et al. 2012a,b), also on board SDO. The AIA and HMI data are processed using standard processing software provided in the solar software (SSW; Freeland & Handy 1998) distribution. The processed level 1.5 AIA and HMI data provides a pixel resolution of 0.6″.

The fan loop system, which is studied here, belongs to the active region NOAA *AR 12553* observed on June 16, 2016. We analysed the AIA observations recorded between 07:30:10 to 10:30:10 UT. We note that all the observations taken in different channels are rotated or de-rotated to the reference time at 9:15:00 UT for further analysis. Panel a in Fig. 1 displays a portion of the Sun's disc image including *AR 12553* observed in 171 Å passband. The yellow box encloses the fan loop system named as region of interest, a zoomed-in version of which is shown in panel b.

3. Data analysis and results

In Fig. 2, we plot the regions of interest observed from HMI and AIA. Panels a and b show the HMI intensity and line-of-sight (LOS) magnetogram, respectively. The magnetogram is displayed within the magnetic field range of ±1000 G (with white indicating positive polarity and black indicating negative polarity). Panels c to i are taken by AIA in passband as labelled. The overplotted cyan inner and yellow outer contours are plotted to visualise the umbra–penumbra and penumbra–plage boundaries, respectively. The umbra–penumbra contour is at the level of 38 000 DN, whereas the penumbra–plage boundary is at the level of 53 000 DN based on HMI continuum image. These contours are also overplotted on the UV and EUV intensity images obtained in 1600 Å and 171 Å, shown in panels c and e. Panel e reveals that some fan loops are rooted deep inside the umbra, and some are at the umbra–penumbra boundary.

Since our primary motivation is to study the wave dynamics of steady fan loops, we focus on the region that does not suffer from any flaring activity. With this condition in mind, we located three different regions on the fan loop system with white boxes, as shown in panel a of Fig. 3, and studied the corresponding light

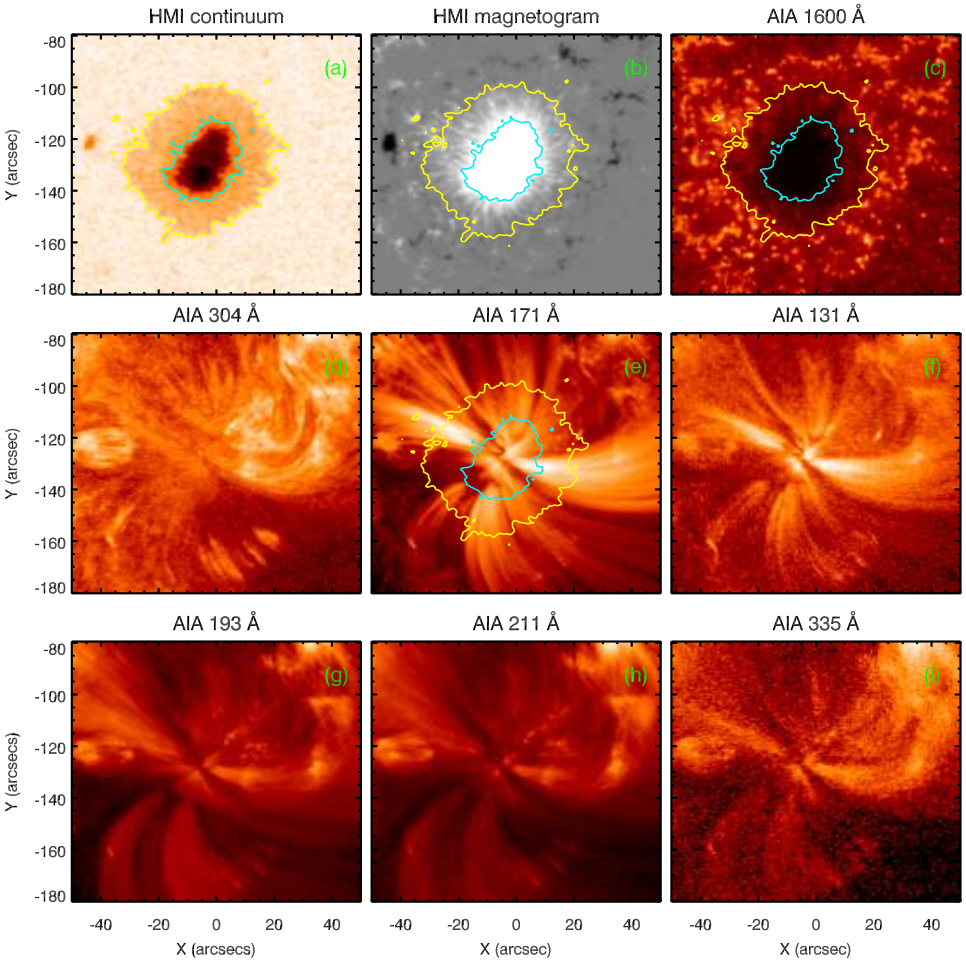

Fig. 2. Regions of interest observed with HMI and AIA at different wavelengths, as labelled. The overlaid cyan and yellow contours in *panels a–e* are the umbra–penumbra and penumbra–outer sunspot boundaries, respectively, obtained from HMI continuum.

curves over the following three-hour period. The resultant light curves are shown in panel b of Fig. 3. The light curves are normalised with respect to the maximum intensities of each curve. The light curves conspicuously give the impression that the fan loop system does not show evolution more than 10% from the mean. Therefore, these could be considered for our study. The blue light curve taken from a location along fan loop 3 indicates some background intensity enhancement from time to time.

In order to study the existence and propagation of intensity disturbances along the fan loops, we employ time-distance analysis and construct artificial slits (slits 1, 2, and 3) along the three fan loops as shown in panel a of Fig. 3. We choose the 171 Å image for the identification of fan loops as they are best seen at temperature of $\log[T/K] = 5.80$ (e.g. Brooks et al. 2011; Ghosh et al. 2017). We note that each slit is four pixels wide. We further note that this analysis could be performed using one slit. However, to check the consistency of the results, we used three different slits along different fan loops anchored in the umbra of the sunspot (see panel a in Fig. 3). We describe the results for slit 1 in the following, and provide the results for slits 2 and 3 in the Appendix for brevity.

3.1. Time-distance maps

Figure 4 displays the time-distance map observed along slit 1 in 171 Å. The time-distance map reveals clear propagation of intensity disturbances in the form of dark and bright ridges. These ridges are observed up to a distance of 8–10″ (5.90–7.35 Mm) along the slit.

Figure 5 displays the time-distance maps obtained along slit 1 from other AIA EUV channels as labelled. The PIDs are clearly discernible in all the EUV channels of AIA except for channels 335 Å and 94 Å, which are formed above a temperature of 2.5 MK. In AIA 193 Å, the PIDs are observed up to a distance of 8–10″ (5.9–7.35 Mm) similar to the 171 Å channel of AIA. However, in channels such as 131 Å and 211 Å, the PIDs are only seen up to a distance of around 4″ (2.9 Mm). The time-distance maps also reveal a decrease in the signal strength of the propagating features as they travel along the loops, which indicates a reduction in their amplitude of oscillations (≈10%–5%).

To perform a quantitative analysis on the propagation of the intensity disturbances, we obtain light curves at different projected heights from the origin of the slit. The yellow dashed lines in Figs. 4 and 5 highlight the locations chosen to receive the light curves. The locations are labelled L1, L2, L3, and L4, which correspond to 1.2″, 3.0″, 4.8″, and 6.6″, respectively. We note that the light curves were obtained from the absolute unprocessed time-distance maps. We show these light curves in 171 Å for a few projected heights in Fig. 6 (left column). In the right column of Fig. 6, we plot corresponding detrended light curves. The overplotted blue lines on the original light curves indicate the background trends, which are obtained from a running average over 30 min. We see that a 30 min running average describes the low-frequency background very well. We then subtract the background trends from the respective original light curves to obtain the detrended light curves. The detrended light curves provide a very clear, evident, and unperturbed evolution of the intensity. We use the detrended light curves for further studies.

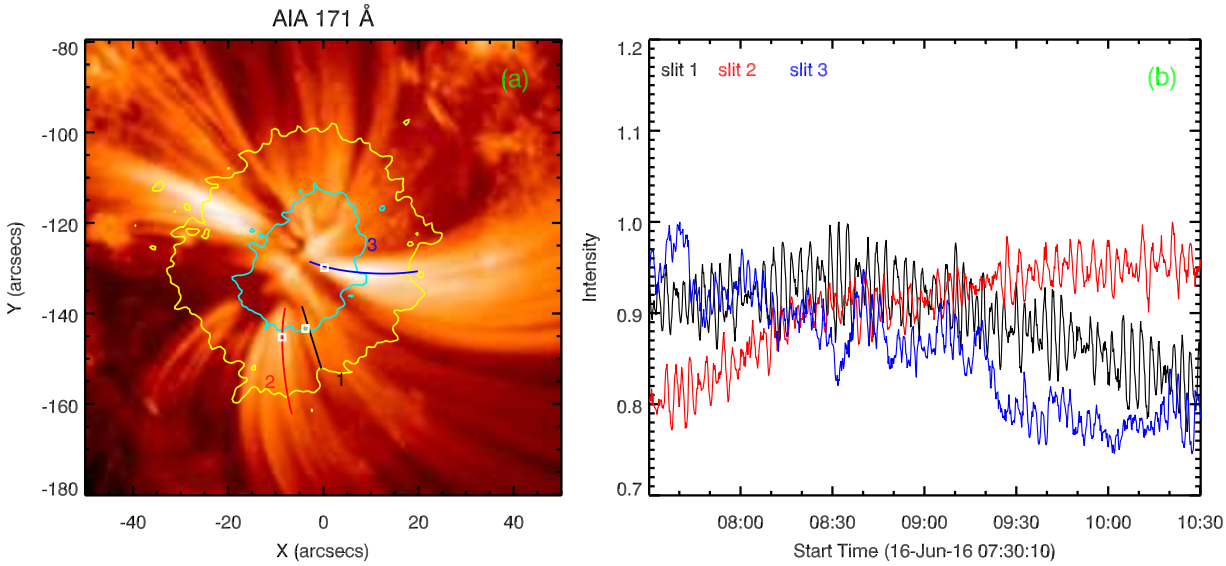

Fig. 3. *Panel a*: fan loop system traced with black, red, and blue curved slits to perform time-distance analysis. The small white boxes locate the region used to study the steadiness of the fan loops. The contours are umbra–penumbra and penumbra–outer sunspot boundaries as described in Fig. 2. *Panel b*: normalised light curves in AIA 171 Å obtained for the white boxes shown in panel a.

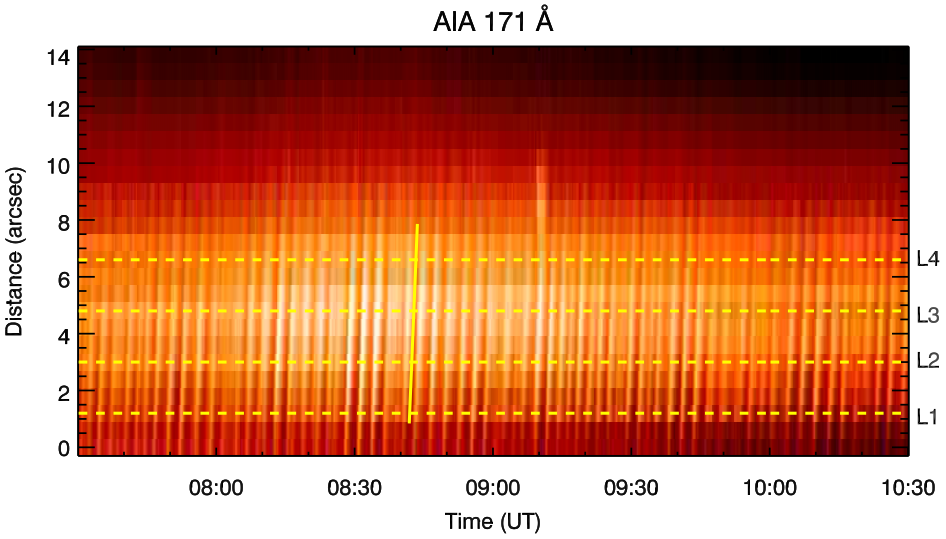

Fig. 4. Time-distance map obtained along artificial slit 1 using 171 Å images. The yellow horizontal dashed lines show the locations used to obtain the light curves for further analysis. The slanted yellow line along the propagating feature is used to estimate average projected speed.

3.2. Phase speeds of the propagating intensity oscillations

Before going into the details of the analysis, we characterise the PIDs in terms of their phase speeds as its measurements play a vital role in understanding their nature. To obtain the phase speeds we employ two methods. In one method, we obtain the phase speeds by getting the slopes of the ridges observed in the time-distance plots. We draw multiple slopes (more than 20) along the propagating ridges by visual inspection and obtained the average propagation speed. The overplotted yellow and white slanted lines in Figs. 4 and 5 indicate the slopes used to measure the average projected phase speeds of the PIDs. We obtain the average projected phase speeds along slit 1 as $50.0 \pm 9.0\,\mathrm{km\,s^{-1}}$ for 171 Å, $50.0 \pm 10.0\,\mathrm{km\,s^{-1}}$ for 131 Å, $57.7 \pm 10.0\,\mathrm{km\,s^{-1}}$ for 193 Å, and $49.0 \pm 13.6\,\mathrm{km\,s^{-1}}$ for 211 Å. The noted errors are the standard deviation obtained using multiple slopes.

Although manually drawing slopes provides a feasible estimate of the phase speeds, it is subject to errors due to its user-dependent nature. Therefore, in order to avoid the human bias associated with this method, we employ a second technique that provides phase speeds by cross-correlating the light curves obtained at different heights (e.g. Gupta et al. 2010; Kiddie et al. 2012). The cross-correlation yields the time lag corresponding to the maximum cross-correlation coefficient and thereby the phase speeds. We carry out this analysis by using the standard IDL routine *c*_correlate. For this purpose, we consider the detrended light curves obtained at locations L1 and L2 (see yellow dashed lines in Figs. 4 and 5). We note that the analysis carried out with the original light curves also gives similar time lags.

The cross-correlation curves obtained for different AIA EUV channels are shown in Fig. 7. The obtained phase speeds are given in Table 1 against different time lags observed in different EUV channels. For comparison, we also list the phase speeds achieved using the ridges of time-distance maps. We note that the obtained phase speeds using the two methods are in agreement within the errors.

The obtained phase speeds are not the true speeds, but are the projected speeds in the plane of sky, as mentioned earlier. In order to measure the true phase speed we need an estimate of the inclination angle (the angle between the line of sight and the

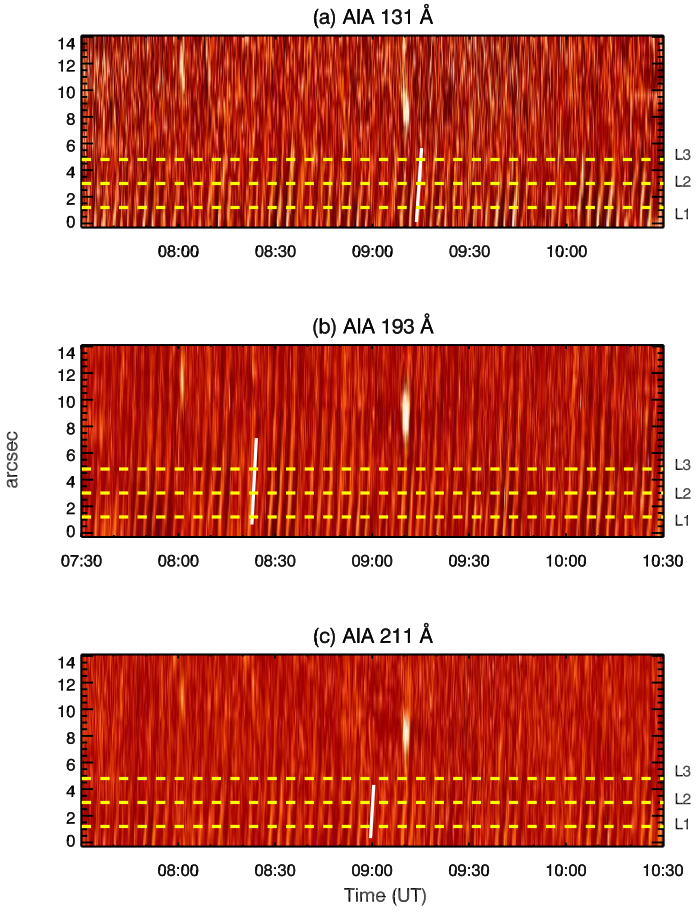

Fig. 5. Time-distance maps obtained along artificial slit 1 in different AIA EUV channels as labelled. The yellow horizontal dashed lines indicate the locations chosen to obtain the light curves for further analysis. The white slanted lines are used to obtain average projected wave speeds, as mentioned in Fig. 4.

guided magnetic field along which the wave propagates). The true phase speed is then obtained from the measured projected phase speed divided by the sine of the inclination angle. Since we do not have a direct measurement of the inclination angle of the guide field, we consider a range of possible angles varying between 10° to 90°, and estimate the respective true phase speeds for different AIA channels. Our findings show that the true phase speeds remain close to the sound speed in corona[1]. The sound speed for 1 MK coronal plasma is around 140 km s^{-1}. As an example, we discuss the estimated true phase speeds of the PIDs in AIA 171 Å channel considering different inclination angles in the Appendix A. The phase speeds of the PIDs closer to the speed of sound suggest that they are slow mode magneto-acoustic waves.

3.3. Amplitude modulation observed in AIA 171 Å

The detrended light curves in 171 Å (Fig. 6) reveal a peculiar oscillatory pattern. We find the clear presence of an amplitude modulation with an overall increase and decrease in the wave pattern over time. The modulation is discernible even in the time-distance map shown in Fig. 4 in terms of brightness.

[1] The speed of sound in the solar corona is given by $0.14T^{1/2}$ km s^{-1} with T measured in kelvin [K] (see Aschwanden 2004).

In order to understand the modulation in greater detail, we obtained the frequency components responsible for these patterns using Fourier analysis and studied their evolution using wavelet analysis (Torrence & Compo 1998).

3.3.1. Fourier analysis

Figure 8 displays the normalised Fourier power spectra derived from the original light curves for locations L1–L4 in Fig. 4 (yellow dashed lines). The power in the panels is normalised with respect to the maximum power obtained at location L1. The power spectra of all the locations indicate three dominant peaks within 5–6 mHz (3.33–2.78 min). They are at around 5.26 mHz (3.17 min, labelled f2 in Fig. 8), 5.56 mHz (3.00 min, f3), and 5.83 mHz (2.85 min, f4). In addition, there are other smaller peaks identified at around 4.99 mHz (3.34 min, f1), 6.11 mHz (2.72 min, f5), 6.84 mHz (2.44 min, f6), and 7.42 mHz (2.24 min, f7). The vertical dashed black lines indicate these peaks. We also observe a decrease in the power of the frequency peaks as we go away from the footpoint of the fan loop.

The observations of several nearby frequencies in the power spectra led us to postulate that the phenomenon of beat may play a role in generating the amplitude modulation. The beat is a phenomenon that occurs when two waves of slightly different frequencies (e.g. f_1 and f_2) interfere, giving rise to a resulting wave undergoing amplitude modulations with frequency $f_b = f_1 - f_2$. We call this frequency beat frequency, f_b. In the current observations, assuming the interaction of the three dominant frequency components (f2, f3, and f4) observed in Fig. 8, we find that for frequency components 5.26 mHz (f2) and 5.83 mHz (f4), there is a beat frequency $f_b = 0.57$ mHz, i.e. ≈29 min. We note that 29 min is close to the modulation period that we obtain from a simple visual inspection of the detrended light curves in Fig. 6 (see also Sect. 3.3.2).

The other combinations give us $f_b = 0.30$ mHz (≈55 min) for 5.26 mHz (f2) and 5.56 mHz (f3), and $f_b = 0.27$ mHz (≈61.70 min) for 5.56 mHz (f3) and 5.83 mHz (f4). Similarly, the interference of the dominant frequency around 5.56 mHz (3 min.) with the frequencies at around 4.99 mHz (f1), 6.11 mHz (f5), 6.84 mHz (f6), and 7.42 mHz (f7), gives rise to beat frequencies of around 0.57 mHz (29 min), 0.55 mHz (30 min), 1.28 mHz (13 min), and 1.86 mHz (8.96 min), respectively. However, we note that in the dynamic and complex solar atmosphere, it is difficult to explain the observed period of amplitude modulation in terms of a particular beat period as the propagation is affected by all the frequency components. Krishna Prasad et al. (2015) observed amplitude modulation in the Fourier-filtered light curves with a mean period of 20–27 min, and reported the possibility of occurrence of the beat. We note that long-period oscillations (periods of around 8 min, 12 min, 24 min, 40 min, and 63.4 min) in coronal fan loops have also been reported by Wang et al. (2009) and Stenborg et al. (2011). However, no observational evidence was provided to explain their origin.

3.3.2. Wavelet analysis

To study the temporal variation of the frequency, we perform wavelet analysis on the 30 min detrended 171 Å light curves obtained at locations marked in Fig. 4. For this purpose, we use the Morlet wavelet as the basis function, which is a plane wave multiplied by a Gaussian, and convolve it with the light curves (Torrence & Compo 1998). In Fig. 9, we plot the wavelet results for the light curves obtained at locations, L1 (left panel) and L3 (right panel). Each wavelet plot consists of three panels.

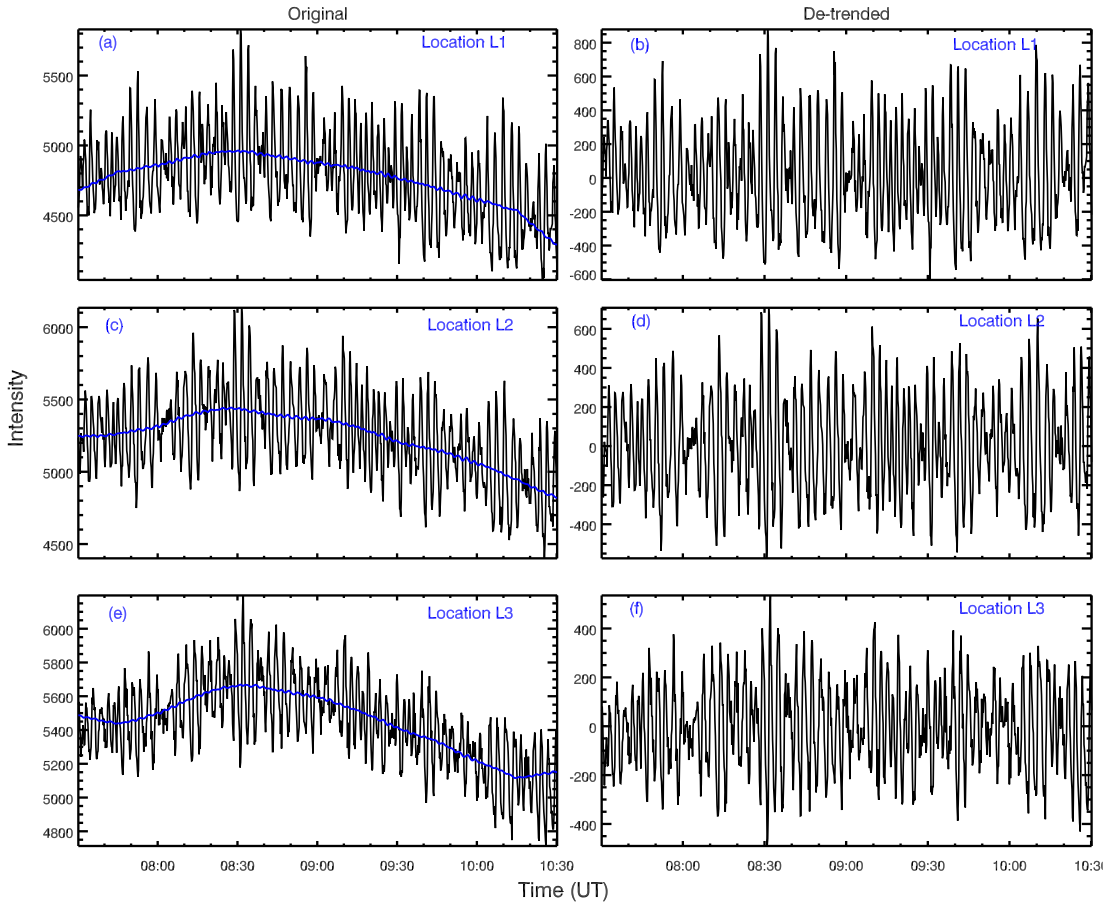

Fig. 6. Original (*left column*) and detrended (*right column*) light curves obtained in AIA 171 Å from different locations, as marked along slit 1. The overplotted blue lines in the *left panels* show the background trend of respective locations.

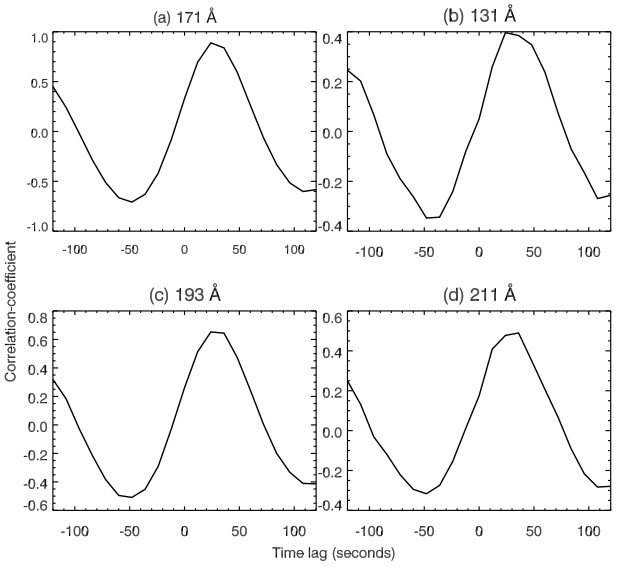

Fig. 7. Cross-correlation analysis performed between detrended light curves obtained from locations L1 and L2 of the time-distance maps (locations shown by yellow dashed lines in Figs. 4 and 5). The cross-correlation coefficient is plotted on the *y*-axis as a function of time lag in seconds on the *x*-axis.

The detrended light curve used for wavelet analysis is displayed in top panel a. The wavelet power spectrum that shows the variation of power at different periods with time is plotted in the bottom left panel b. The global wavelet power spectrum, obtained by taking the average over the time domain of the wavelet transform, is plotted in the bottom right panel c. In each wavelet spectrum (lower left panel), we denote a cross-hatched region called the cone of influence (COI). The COI region appears because of the edge effects which arises due to the finite length of time series. Any estimate of the oscillation period in this region becomes unreliable. The horizontal dashed lines in the global wavelet panels show the longest period that can be detected due to COI. We mention the first two power peaks (P1 and P2) obtained from the global wavelet at the right top corner of the wavelet plots.

In the wavelet spectrum panels, we find that most of the oscillating power lies in the range 2–4 min throughout the observed duration. We also observe an increase and decrease in the wavelet power, which is co-temporal with the appearance and disappearance of the modulations observed in the corresponding light curves. As expected, the global wavelet spectra show the presence of dominant power peak (P1) at around 3 min period for all the locations. We obtain second power peaks (P2) around 57.68 min. and 44.48 min. for locations L1 and L2, and at 28.84 min and 20.30 min for locations L3 and L4, respectively. We see that these second power peaks are below the 99% confidence level, and therefore are unreliable.

To quantify the modulation period, we follow a particular approach (Krishna Prasad et al. 2015; Sharma et al. 2017). We see that it is the 3 min wave amplitude that is modulated. The Fourier power spectra (Fig. 8) also illustrate significant power within 2–4 min, with dominant peaks around 3 min. Inspecting the power within 2–4 min, we measure the wavelet oscillatory

Table 1. Phase speeds of the PIDs in different EUV channels obtained from cross-correlation analysis.

AIA EUV channel Å	Time lag sec.	Phase speed from cross-correlation analysis km s^{-1}	Phase speed from time-distance ridges km s^{-1}
171	24.3	54.44	50.0
131	24.4	54.22	50.0
193	24.4	54.22	57.7
211	35.55	37.21	49.0

Notes. Phase speeds obtained using the ridges of time-distance measurements are also presented for better comparison.

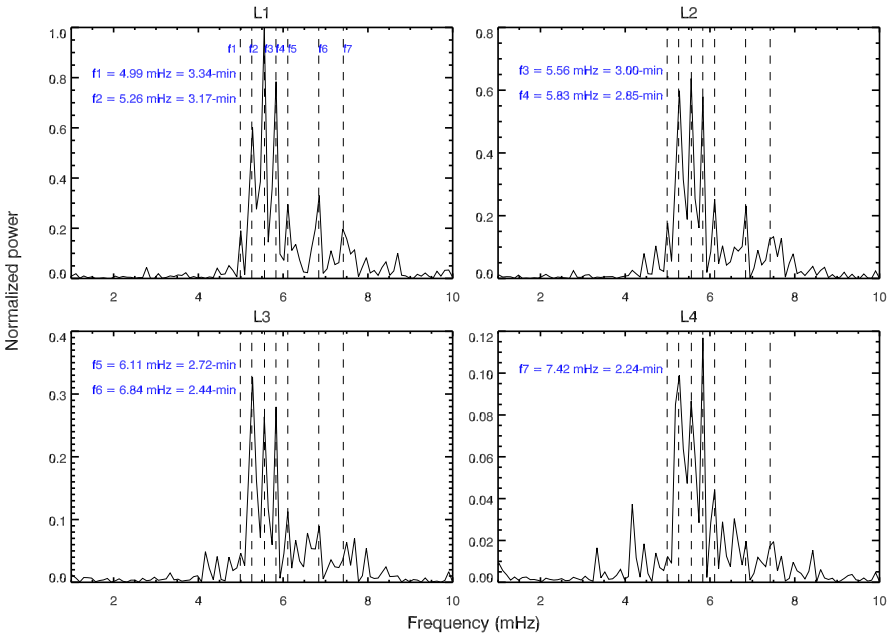

Fig. 8. Fourier power spectrum of the original light curves obtained from different locations of AIA 171 Å time-distance map (locations marked in Fig. 4).

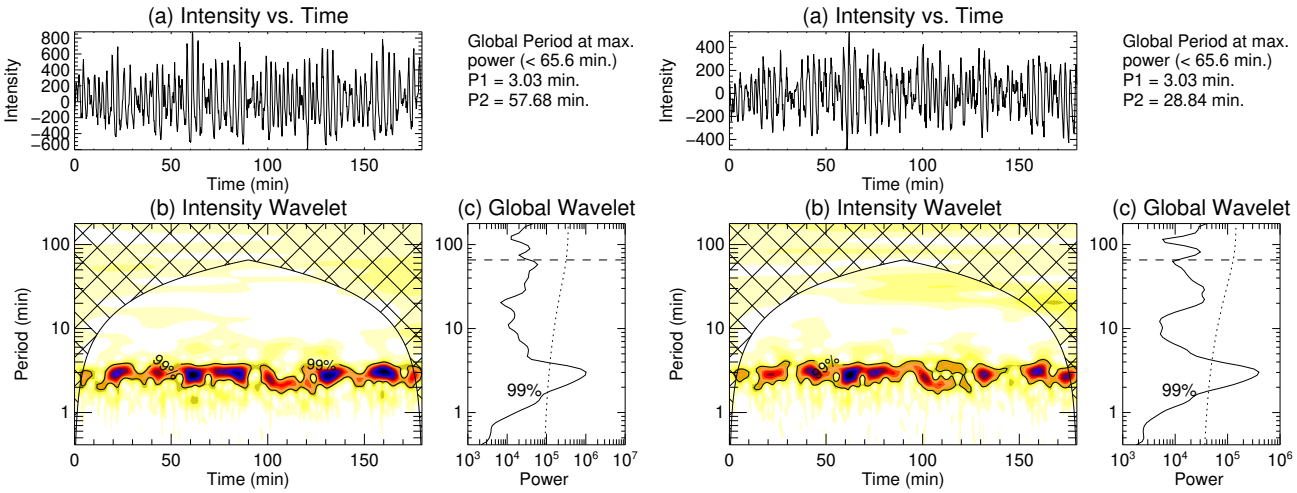

Fig. 9. Wavelet analysis results of detrended light curves obtained from slit 1 AIA 171 Å time-distance map for locations L1 (*left*) and L3 (*right*) (location given in Fig. 4). *Top panel*: variation of obtained detrended intensity with time. *Bottom left panel*: corresponding wavelet spectrum (high power density in blue). *Bottom right panel*: global wavelet power spectrum. The dashed lines indicate the maximum period detectable from wavelet analysis due to cone-of-influence, whereas the dotted line indicates 99% confidence level curve. Periods P1 and P2 of the first two global power peaks are printed at the top right. On the time axis, the time starts at 7:30 UT.

power averaged within this period range. This oscillatory power will essentially mimic an amplitude variation that would be caused by all the waves having periods within the 2- and 4 min range (Sharma et al. 2017; Krishna Prasad et al. 2015; Sych et al. 2012). Then we apply wavelets to the obtained amplitude variation to estimate the dominant period of amplitude modulation. Figure 10 shows wavelet power spectra obtained in such way for AIA 171 Å for locations, as done for Fig. 9. We obtain the dominant or first power peaks (P1) around 34.30 min, 20.39 min, 22.24 min, and 26.45 min for locations L1, L2, L3,

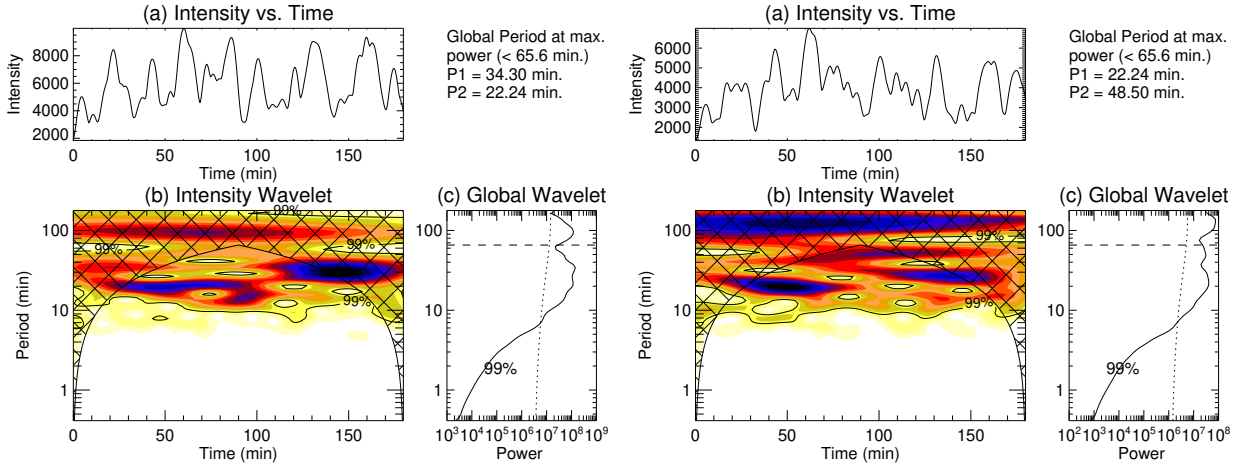

Fig. 10. Wavelet analysis result of 171 Å light curves obtained by averaging waves with oscillation periods in the range 2–4 min. Wavelet plots are obtained for similar locations, L1 (*left*) and L3 (*right*), as mentioned in Fig. 9.

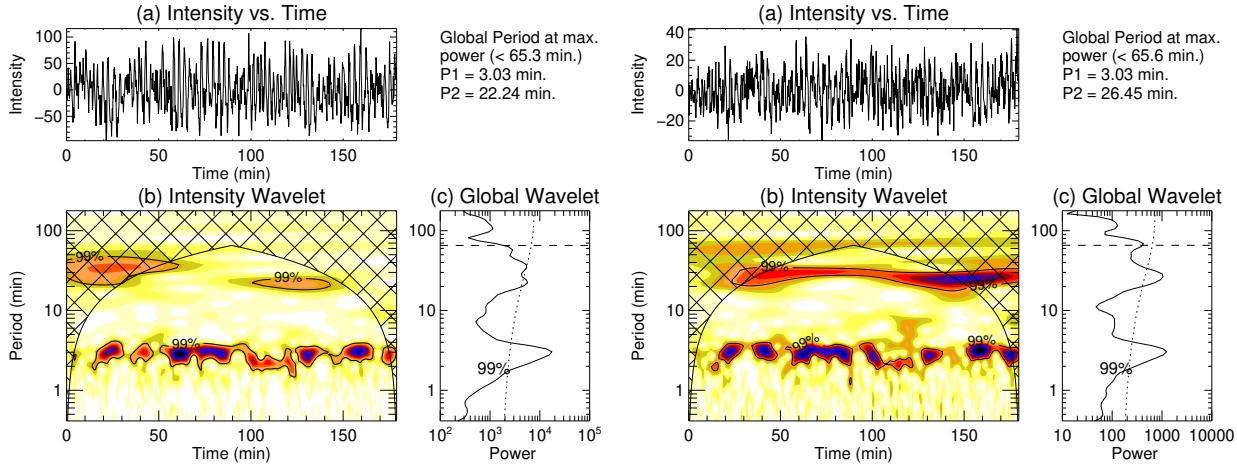

Fig. 11. Wavelet analysis results of detrended light curves observed in AIA 193 Å (*left*) and AIA 211 Å (*right*) for location L1 of the time-distance maps (shown in Fig. 5). The panels are described in Fig. 9.

and L4, respectively. We find the longer-period power peaks above the 99% confidence level for all the marked locations of Fig. 4. We note that we find similar results with the unfiltered original light curves.

3.4. Amplitude modulation in other AIA EUV channels

For completeness, we study the light curves obtained from other AIA EUV channels at the locations shown by overplotted yellow dashed lines in Fig. 5. We detrended the light curves as was done for those obtained from 171 Å, and performed further analysis. In Fig. 11 we present the wavelet analysis results obtained using the light curve at L1 for 193 Å (left panels) and 211 Å (right panels). The power is concentrated at a period (P1) of around 3 min, and undergoes an increase and decrease over time, as can be seen in the panels b of Fig. 11. To quantify the modulation period, we used a method similar to that used for AIA 171 Å (see last paragraph of Sect. 3.3.2). We obtain the dominant power peaks (P1) around 22.24 min and 20.39 min for 193 Å and 211 Å, respectively. The analysis of 131 Å showed similar behaviour and provided the dominant modulation period around 22.24 min. However, we note that the modulation is best seen in AIA 171 Å.

3.5. AIA 1600 Å and 304 Å observations at the footpoint of the fanloop

To investigate the origin of the modulation shown by the propagating slow MHD waves in AIA EUV channels, we study the footpoint of the fan loop in AIA 1600 Å and 304 Å. Figure 12 shows an AIA 1600 Å image with the footpoint of the fan loop obtained from AIA 171 Å traced by slit 1. A yellow box bounds the footpoint location situated in the sunspot umbra. The size of the box is 4×4 in pixel scale. We obtain the light curves averaged over the region and detrend it over 30 min and performed wavelet analysis. The wavelet results for 1600 Å (left panel) and 304 Å (right panel) are shown in Fig. 13. In the wavelet power map, we do not observe a clear pattern in 1600 Å, whereas in 304 Å there is clear modulation around 3 min. We obtain the modulation period around 22.24 min in the same way as obtained for 171 Å (see last paragraph of Sect. 3.3.2).

3.6. Observation of high-frequency component

Besides the modulation, we observe some high-frequency oscillations around 1.5 min (≈11 mHz) in the wavelet power maps (panel b). We show zoomed-in versions of the wavelet power

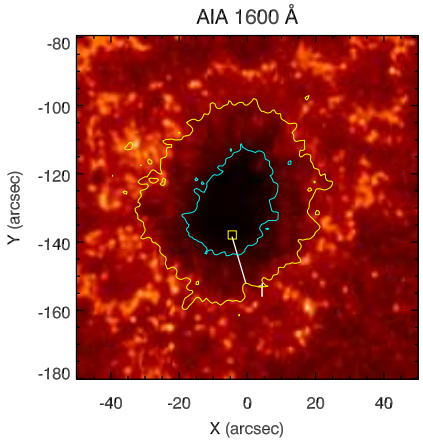

Fig. 12. Sunspot umbra in AIA 1600 Å. The overplotted yellow box corresponds to the region at the footpoint of slit 1. The light curves averaged over the region are considered for further analysis in the chromospheric channels, e.g. AIA 304 Å and 1600 Å. Contours are similar to those described in panel a of Fig. 3.

panels b in Fig. 14 for different AIA channels as labelled. These powers are observed at the footpoint of the fan loop in the sunspot umbra (Fig. 12) at 304 Å, and at location L1 of the fan loops for the coronal channels 171 Å, 193 Å, and 211 Å. However, they are not present throughout the time series. In addition, we note that we detect the high-frequency components at the 90% confidence level. Therefore, further observational work is required to establish the viability of this finding.

4. Summary and conclusions

In this work, we have studied the nature of PIDs observed in an active region fan loop system rooted in a sunspot umbra using AIA/SDO observations. We find that the PIDs are best observed in 171 Å data. The PIDs were also seen in other channels of AIA except for 335 Å and 94 Å. We have measured the phase speeds of the PIDs in all the AIA channels and found that the phase speeds are subsonic. This is suggestive that these are slow-mode magneto-acoustic waves. We further found that the phase speeds measured in different channels are not dependent on temperature. This is in contradiction with the results obtained by Banerjee et al. (2009), Krishna Prasad et al. (2012), Kiddie et al. (2012), and Gupta (2014). A possible reason for this may be the broad temperature response of the AIA channels. Fan loops are structures of typically 1 MK; therefore, it may be that the emissions from the lower-temperature components are contributing to these different AIA EUV emissions (Ghosh et al. 2017), thereby giving similar phase speeds.

Our result shows that the PIDs have longer detection length (≈5.9−7.35 Mm) in 171 Å and 193 Å, whereas a shorter detection length (≈2.9 Mm) in 131 Å and 211 Å. The similar detection length in 171 and 193 Å could be due to the similar temperature range covered by these two channels. We note that AIA 131 Å has a peak formation temperature closer to that of 171 Å in quiet conditions. Therefore, the shorter detection length observed in 131 Å may be due to the weaker signal-to-noise ratio (S/N) (<10) than that of 171 Å (>65). The shorter detection length observed in 211 Å channel may also be related to its S/N, which we find to be less than 20.

The light curves obtained at multiple locations along the loops show an increase and decrease in the amplitude of oscillations over time. This variation is more clearly seen in the detrended light curves (see Fig. 6). Fourier analysis of the original light curves reveal that there are several nearby frequencies within 5–8 mHz. The findings obtained here suggest that beat may be a possible explanation for the observed amplitude modulation, very likely created due to the interference of the nearby frequency components. We observe similar frequency peaks in all the AIA EUV coronal (except AIA 335 Å and 94 Å) and chromospheric channels. Lites (1986) has reported the various frequency peaks identified in our study in chromospheric umbra, and Fludra (2001) reported them in transition region sunspot plumes. Centeno et al. (2006, 2009) and Krishna Prasad et al. (2015) observed the presence of amplitude modulations in Fourier filtered light curves and measured a modulation period of 20–27 min (Krishna Prasad et al. 2015). However, in our study, the amplitude modulations were prominent enough to detect them prior to any filtration (Fig. 6), which to our knowledge is the first such observational finding. Wavelet analysis also reveals an increase and decrease in the oscillation power around 3 min simultaneous with the observed amplitude modulation. We obtain a modulation period in the range of 20–30 min.

A similar amplitude variation at the lower solar atmosphere (right panels of Fig. 13), as observed by AIA 304 Å ($\log[T/K] = 4.7$; Lemen et al. 2012) supports one more possibility: the amplitude variability may be caused by the underlying driver. Photospheric p-modes are, in general, assumed to be the cause of propagating slow magneto-acoustic waves observed in the corona (De Pontieu et al. 2005; Krishna Prasad et al. 2015; Zhao et al. 2016). Hence, the amplitude variability of the p-mode may affect and give rise to the particular amplitude variation of the propagating intensity waves observed along the fan loop. Observational studies have shown the effect of oscillatory phenomena in the lower solar atmosphere on the propagation of slow magneto-acoustic waves along coronal fan loops (Jess et al. 2012; Sharma et al. 2017). However, further study is required both observationally and theoretically to understand the origin of such amplitude modulation in time series.

In addition to the amplitude modulation, we see low-period (high-frequency) oscillations around 1.5 min (11 mHz) (see Fig. 14) in this study. We observe these high-frequency oscillations both at the chromospheric and coronal heights. Wang et al. (2018) first observed high-frequency oscillations by imaging observations at different heights above sunspot umbra in the range 10–14 mHz (around 1 min). They related such high-frequency modes at coronal heights to perturbations at photospheric umbra. Krishna Prasad et al. (2017) reported frequencies around 13 mHz using IRIS 2796 Å in chromospheric sunspot umbra. We note that the observed high frequency around 11 mHz is close to two times that of the dominant (fundamental) frequency at around 5.56 mHz, and hence is similar to the second harmonics. However, caution should be taken when associating the high-frequency modes observed in our study with second harmonics, as harmonics have been observed in standing waves in coronal closed loops (Srivastava & Dwivedi 2010). Verwichte et al. (2004) reported the detection of higher harmonics in coronal kink wave oscillations with a deviation in the frequency ratio of second to first harmonics from its canonical value of 2 in a homogeneous medium. Andries et al. (2005), Erdélyi & Verth (2007) and Luna-Cardozo et al. (2012) proposed that this deviation may occur because of longitudinal density and/or magnetic stratification along expanding flux tubes like those in the corona, and therefore can be used as a seismological tool to measure the density scale height.

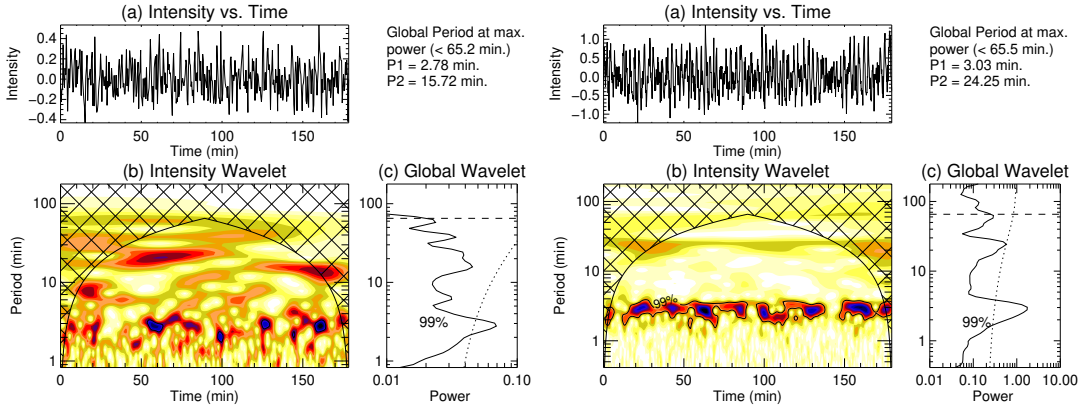

Fig. 13. Wavelet analysis of the detrended light curves extracted from the yellow box location in Fig. 12. *Left panels* are obtained from 1600 Å, and *right panels* from 304 Å. The panels are described in Fig. 9.

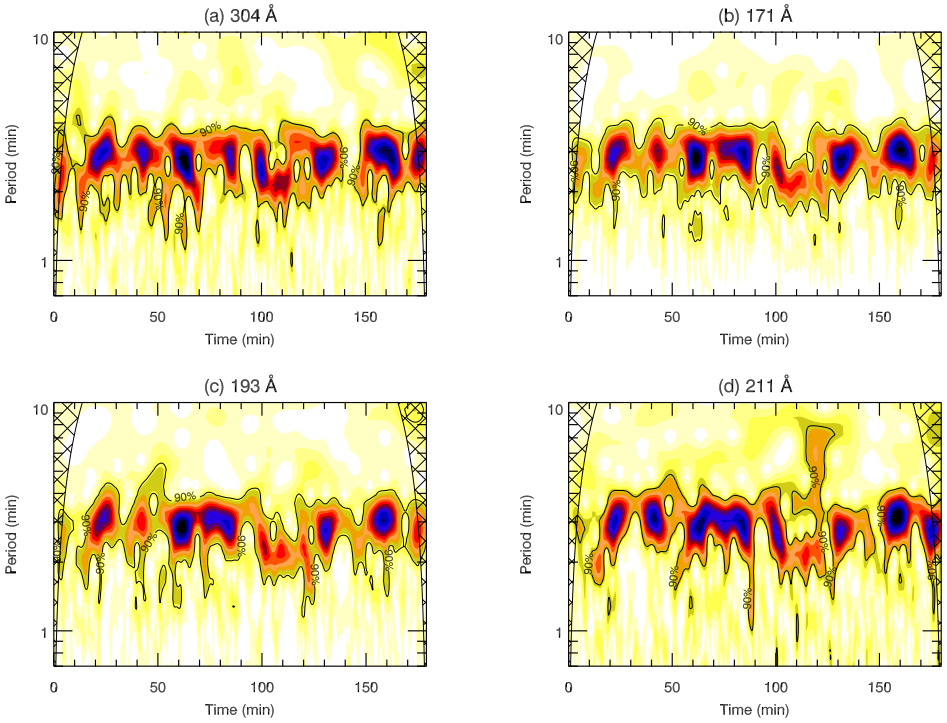

Fig. 14. Zoomed-in images of different wavelet power maps. *Panel a* is taken from right side of Fig. 13. *Panel b* is from the left side of Fig. 9, and *panels c and d* are from Fig. 11.

Acknowledgements. The authors are thankful to the referee for relevant suggestions on improving the manuscript. A. S. and D. T. acknowledge the Max-Planck Partner Group of the Max-Planck Institute for Solar System Research, Göttingen at IUCAA. R. E. is grateful to Science and Technology Facilities Council (STFC Grant nr ST/M000826/1) UK and to Chinese Academy of Sciences President's International Fellowship Initiative, Grant No. 2019VMA0052 for the support received. G. A. Ahmed acknowledges the visiting associateship of IUCAA. AIA and HMI data used here, are courtesy of SDO (NASA).

References

Andries, J., Arregui, I., & Goossens, M. 2005, ApJ, 624, L57
Aschwanden, M. J. 2004, Physics of the Solar Corona. An Introduction (Praxis Publishing Ltd)
Banerjee, D., Teriaca, L., Gupta, G. R., et al. 2009, A&A, 499, L29
Berghmans, D., & Clette, F. 1999, Sol. Phys., 186, 207
Boerner, P., Edwards, C., Lemen, J., et al. 2012, Sol. Phys., 275, 41
Bogdan, T. J. 2000, Sol. Phys., 192, 373
Bogdan, T. J., & Judge, P. G. 2006, Philos. Trans. R. Soc. London Ser. A, 364, 313
Brooks, D. H., Warren, H. P., & Young, P. R. 2011, ApJ, 730, 85
Centeno, R., Collados, M., & Trujillo Bueno, J. 2006, ApJ, 640, 1153
Centeno, R., Collados, M., & Trujillo Bueno, J. 2009, ApJ, 692, 1211
Chandra, R., Gupta, G. R., Mulay, S., & Tripathi, D. 2015, MNRAS, 446, 3741
Cranmer, S. R. 2009, Liv. Rev. Sol. Phys., 6, 3
Culhane, J. L., Harra, L. K., James, A. M., et al. 2007, Sol. Phys., 243, 19
Delaboudinière, J., Artzner, G. E., Brunaud, J., et al. 1995, Sol. Phys., 162, 291
Del Zanna, G., O'Dwyer, B., & Mason, H. E. 2011, A&A, 535, A46
De Moortel, I. 2009, Space Sci. Rev., 149, 65
De Moortel, I., Ireland, J., & Walsh, R. W. 2000, A&A, 355, L23
De Moortel, I., Hood, A. W., Ireland, J., & Walsh, R. W. 2002a, Sol. Phys., 209, 89
De Moortel, I., Ireland, J., Hood, A. W., & Walsh, R. W. 2002b, A&A, 387, L13
De Moortel, I., Ireland, J., Walsh, R. W., & Hood, A. W. 2002c, Sol. Phys., 209, 61
De Pontieu, B., Erdélyi, R., & James, S. P. 2004, Nature, 430, 536
De Pontieu, B., Erdélyi, R., & De Moortel, I. 2005, ApJ, 624, L61
Erdélyi, R. 2004, Astron. Geophys., 45, 4.34
Erdélyi, R., & Verth, G. 2007, A&A, 462, 743
Fludra, A. 2001, A&A, 368, 639
Freeland, S. L., & Handy, B. N. 1998, Sol. Phys., 182, 497
Ghosh, A., Tripathi, D., Gupta, G. R., et al. 2017, ApJ, 835, 244
Gupta, G. R. 2014, A&A, 568, A96
Gupta, G. R., Banerjee, D., Teriaca, L., Imada, S., & Solanki, S. 2010, ApJ, 718, 11
Gupta, G. R., Teriaca, L., Marsch, E., Solanki, S. K., & Banerjee, D. 2012, A&A, 546, A93

Handy, B. N., Acton, L. W., Kankelborg, C. C., et al. 1999, Sol. Phys., 187, 229
Jess, D. B., De Moortel, I., Mathioudakis, M., et al. 2012, ApJ, 757, 160
Khomenko, E., & Collados, M. 2015, Liv. Rev. Sol. Phys., 12
Kiddie, G., De Moortel, I., Del Zanna, G., McIntosh, S. W., & Whittaker, I. 2012, Sol. Phys., 279, 427
Kohl, J. L., Esser, R., Gardner, L. D., et al. 1995, Sol. Phys., 162, 313
Kosugi, T., Matsuzaki, K., Sakao, T., et al. 2007, Sol. Phys., 243, 3
Krishna Prasad, S., Banerjee, D., & Singh, J. 2012, Sol. Phys., 281, 67
Krishna Prasad, S., Jess, D. B., & Khomenko, E. 2015, ApJ, 812, L15
Krishna Prasad, S., Jess, D. B., Van Doorsselaere, T., et al. 2017, ApJ, 847, 5
Lemen, J. R., Title, A. M., Akin, D. J., et al. 2012, Sol. Phys., 275, 17
Lites, B. W. 1986, ApJ, 301, 992
Liu, J., Nelson, C., Snow, B., Wang, Y., & Erdélyi, R. 2019, Nat. Commun., 10,
Luna-Cardozo, M., Verth, G., & Erdélyi, R. 2012, ApJ, 748, 110
Marsh, M. S., Walsh, R. W., & Plunkett, S. 2009, ApJ, 697, 1674
Nakariakov, V. M., Verwichte, E., Berghmans, D., & Robbrecht, E. 2000, A&A, 362, 1151
O'Dwyer, B., Del Zanna, G., Mason, H. E., Weber, M. A., & Tripathi, D. 2010, A&A, 521, A21
Ofman, L. 2005, Space Sci. Rev., 120, 67
Ofman, L., Romoli, M., Poletto, G., Noci, G., & Kohl, J.L. 1997, ApJ, 491, L111
Pesnell, W. D., Thompson, B. J., & Chamberlin, P. C. 2012, Sol. Phys., 275, 3
Rajaguru, S. P., Sangeetha, C. R., & Tripathi, D. 2019, ApJ, 871, 155
Reale, F. 2010, Liv. Rev. Sol. Phys., 7, 5
Roberts, B. 2006, Philos. Trans. R. Soc. London Ser. A, 364, 447
Schou, J., Borrero, J. M., Norton, A. A., et al. 2012a, Sol. Phys., 275, 327
Schou, J., Scherrer, P. H., Bush, R. I., et al. 2012b, Sol. Phys., 275, 229
Sharma, A., Gupta, G. R., Tripathi, D., Kashyap, V., & Pathak, A. 2017, ApJ, 850, 206
Srivastava, A. K., & Dwivedi, B. N. 2010, New Astron., 15, 8
Stenborg, G., Marsch, E., Vourlidas, A., Howard, R., & Baldwin, K. 2011, A&A, 526, A58
Sych, R., Zaqarashvili, T. V., Nakariakov, V. M., et al. 2012, A&A, 539, A23
Taroyan, Y., & Erdélyi, R. 2009, Space Sci. Rev., 149, 229
Torrence, C., & Compo, G. P. 1998, Bull. Am. Meteorol. Soc., 79, 61
Verwichte, E., Nakariakov, V. M., Ofman, L., & Deluca, E. E. 2004, Sol. Phys., 223, 77
Wang, F., Deng, H., Li, B., et al. 2018, ApJ, 856, L16
Wang, T. J., Ofman, L., Davila, J. M., & Mariska, J. T. 2009, A&A, 503, L25
Zhao, J., Felipe, T., Chen, R., & Khomenko, E. 2016, ApJ, 830, L17

Appendix A: True phase speeds of PIDs in AIA 171 Å

Table A.1. True phase speeds of PIDs in AIA 171 Å obtained by considering different inclination angles.

Projected phase speed in AIA 171 Å	Inclination angle	Probable true phase speeds
v [km s^{-1}]	θ [°]	v_{ph} [km s^{-1}]
52.9	10	304.6
	20	154.66
	30	105.8
	40	82.29
	50	69.05
	60	61.08
	70	56.29
	80	53.71
	90	52.9

Appendix B: PIDs along slits 2 and 3

We analyse the evolution of intensity disturbances propagating along slits 2 and 3 (shown in Fig. 3a). We find the 3 min propagating intensity oscillations along slits 2 and 3 undergoing amplitude modulations. However, the modulations were not strong enough, as observed for slit 1. Figures B.2 and B.3 present the increase and decrease in wavelet power of the 3 min oscillations representing the modulations.

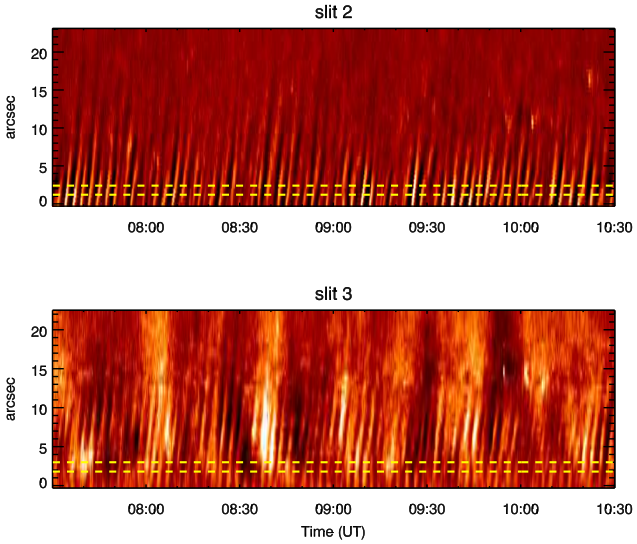

Fig. B.1. Time-distance maps obtained along slits 2 and 3 in AIA 171 Å. Clear propagation of intensity oscillations along the slits are observed. The regions averaged between the overlaid yellow dashed lines are taken for further analysis.

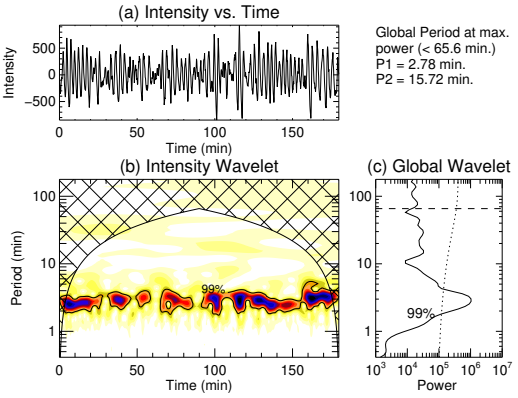

Fig. B.2. Wavelet analysis of intensity disturbances propagating along slit 2. The light curve used for the wavelet analysis is obtained from the region averaged between the yellow dashed lines of Fig. B.1 (top panel: slit 2) in AIA 171 Å. The different panels are described in Fig. 9.

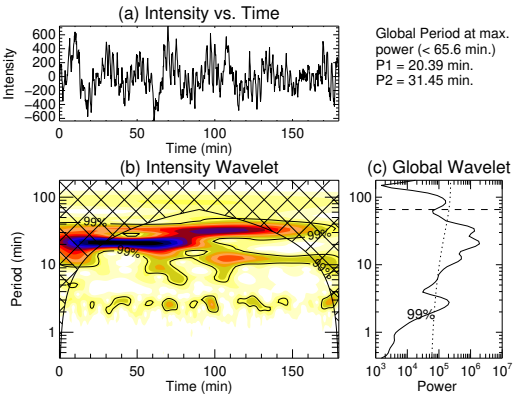

Fig. B.3. Wavelet analysis of PIDs observed along slit 3 in AIA 171 Å. The light curves shown in the *top panel* correspond to the region averaged between the yellow dashed lines of Fig. B.1 (bottom panel: slit 3). The different panels are described in Fig. 9.